

Power Spectrum of Atmospheric Scintillation for the Deep Space Network Goldstone Ka-Band Downlink

C. Ho¹ and A. Wheelon²

Dynamic signal fluctuations due to atmospheric scintillations may impair the Ka-band (around 32-GHz) link sensitivities for a low-margin Deep Space Network (DSN) receiving system. The ranges of frequency and power of the fast fluctuating signals (time scale < 1 min) are theoretically investigated using the spatial covariance and turbulence theory. Scintillation power spectrum solutions are derived for both a point receiver and a finite-aperture receiver. The aperture-smoothing frequency (ω_s), corner frequency (ω_c), and damping rate are introduced to define the shape of the spectrum for a finite-aperture antenna. The emphasis is put on quantitatively describing the aperture-smoothing effects and graphically estimating the corner frequency for a large aperture receiver. Power spectral shapes are analyzed parametrically in detail through both low- and high-frequency approximations. It is found that aperture-averaging effects become significant when the transverse correlation length of the scintillation is smaller than the antenna radius. The upper frequency or corner frequency for a finite-aperture receiver is controlled by both the Fresnel frequency and aperture-smoothing frequency. Above the aperture-smoothing frequency, the spectrum rolls off at a much faster rate of $\exp(-\omega^2/\omega_s^2)$, rather than $\omega^{-(8/3)}$, which is customary for a point receiver. However, a relatively higher receiver noise level can mask the fast falling-off shape and make it hard to be identified. We also predict that when the effective antenna radius $a_r \leq 6$ m, the corner frequency of its power spectrum becomes the same as that for a point receiver. The aperture-smoothing effects are not obvious. We have applied these solutions to the scenario of a DSN Goldstone 34-m-diameter antenna and predicted the power spectrum shape for the receiving station. The maximum corner frequency for the receiver (with $\omega_s = 0.79\omega_0$) is found to be 0.44 Hz (or $1.0\omega_0$), while the fading rate (or fading slope) is about 0.06 dB/s.

¹ Communications Systems and Research Section.

² California Institute of Technology, Trustee, Pasadena, California, pro bono consultant to JPL.

The research described in this publication was carried out by the Jet Propulsion Laboratory, California Institute of Technology, under a contract with the National Aeronautics and Space Administration.

I. Introduction

The Earth's atmosphere and weather impose much larger degradation effects on a Ka-band (around 32-GHz) link than on other lower-frequency bands. On the one hand, the atmosphere can have higher attenuations due to gaseous absorption (water vapor and oxygen), rain, and cloud attenuations with slow fading ($>\text{min}$). On the other hand, the atmospheric turbulences and irregularities under the clear weather condition also can cause fast amplitude fluctuations ($<\text{min}$) due to diffraction and scattering [1–3].

A higher data rate implies a new sensitivity to short-term amplitude (signal-to-noise ratio, SNR) fluctuations. When the wavelength of Ka-band radio waves is comparable to the Fresnel length for atmospheric paths, fast scintillation (0.1–10 Hz) and scattering become significant. Received signals appear highly dynamic as to their amplitude and phase. These fast variations are quite different from the slow variations of amplitude and phase caused by rain or cloud attenuations. Fast variations are superimposed on top of slow fading, causing deep fading in a short time. Both fading frequency (duration) and fading depth (intensity) can determine the fading slopes, which directly affect the times of loss-of-lock and recovery and the short-term dynamics of the systems.

The time series of signal amplitude and frequency spectrum provide two different but equivalent descriptions for the signal variability. The amplitude changes in a time domain can be transferred into a frequency domain through the Fourier transform. The spectral analysis will clearly show the frequency ranges of amplitude changes and the power distributions. Spectrum shapes and damping rates can be significantly different between a finite-aperture antenna and a point antenna. The temporal spectrum of amplitude scintillation depends on the frequency of microwave signals, wind speed, Fresnel length of the path, and antenna aperture.

A study of the antenna aperture effect on power spectrum and frequency range is needed for the Deep Space Network (DSN) large antenna downlink scenario, and it is the central topic of this article. Through this study, we attempt to understand the following questions: How fast can amplitude fluctuations be caused by atmospheric eddies? What are the frequency ranges of the power spectrum for these fluctuations, and what is the upper frequency which directly affects the sample data rate for future Ka-band experiment and telemetry operation? How does the antenna aperture affect the frequency range of signal scintillation? What is the roll-off rate in the high-frequency part of the power spectrum? Is it still the same for the $-8/3$ power law as for a point receiver or is it faster damping? These questions have never been completely solved for a finite-aperture receiver because of their complexity.

In this study, we will first set up the relationship between the temporal covariance and the spatial covariance by using Taylor's hypothesis, which assumes frozen irregularities convected by a steady wind. Then we will convolve the spatial covariance into the power spectrum using the Fourier transform, because the spatial covariance is nothing other than the amplitude variance for scintillation intensity investigated in our companion article in this issue [4]. The complete analytic solutions for the power spectrum are applied to a point receiver first, and then to a receiver with a finite aperture by spatial averaging over the entire antenna aperture. We will further introduce the aperture-smoothing frequency, corner frequency, and damping rate to define the shape of the spectrum for a large aperture antenna. We will perform a detailed analysis on the complicated spectrum by studying its low-frequency and high-frequency approximation solutions and by comparing the spectrum of a finite-aperture antenna with one of a point antenna. Finally, we apply these analytic solutions to the DSN Goldstone 34-m antenna to predict the power spectrum and frequency range of the received signal. A comparison also is made with available Ka-band experiments from small antennas. This study will guide us in modifying the models developed from previous experiments for use on large antennas.

II. Spatial Covariance and Power Spectrum

The power spectrum is an important quantity in describing the variability of random fluctuating signals for a Ka-band receiving system. Power spectrum, $W_\chi(\omega)$, and temporal covariance, $B_\chi(\tau)$, of amplitude scintillations are a Fourier transform pair in the $t \longleftrightarrow \omega$ domain [1–3] given by the following:

$$W_\chi(\omega) = \int_{-\infty}^{\infty} \langle \chi(t) \chi(t + \tau) \rangle e^{i\omega\tau} d\tau \quad (\text{Np})^2 / \text{Hz} \quad (1)$$

$$B_\chi(\tau) = \frac{1}{2\pi} \int_{-\infty}^{\infty} W_\chi(\omega) e^{-i\omega\tau} d\omega \quad (\text{Np})^2 \quad (2)$$

where temporal covariance is defined as $B_\chi(\tau) = \langle \chi(r, t) \chi(r, t + \tau) \rangle$, and $\chi(r, t)$ is the temporal logarithmic amplitude change. Taking Taylor's frozen field assumption that all of the time changes in $f(\mathbf{r}, t)$ are associated with a simple translation of a spatial field distribution with a constant horizontal wind with velocity \mathbf{v}_\perp (where we have assumed that wind velocity fluctuation is negligible), that is,

$$\Delta\rho = \mathbf{v}_\perp \tau$$

and

$$f(\mathbf{r}, t + \tau) = f(\mathbf{r} - \mathbf{v}_\perp \tau, t)$$

we thus have

$$\langle \chi(r, t) \chi(r, t + \tau) \rangle = \langle \chi(r, t) \chi(r + v_\perp \tau, t) \rangle = \langle \chi(r, t) \chi(r', t) \rangle \quad (3)$$

where

$$\mathbf{r}' = \mathbf{r} + \Delta\rho = \mathbf{r} + \mathbf{v}_\perp \tau$$

Thus, the temporal covariance $B_\chi(\tau)$ is equivalent to the spatial covariance $B_\chi(\Delta\rho)$. We will establish the relationship between them as follows:

$$B_\chi(\tau) = \langle \chi(r, t) \chi(r, t + \tau) \rangle = B_\chi(\Delta\rho) = \langle \chi(r) \chi(r + \Delta\rho) \rangle = B_\chi(v_\perp \tau) \quad (4)$$

From the spatial covariance derived in Appendix B in [4], we have the following expression for a case of weak scattering:

$$\begin{aligned} \langle \chi(r, t) \chi(r, t + \tau) \rangle &= \langle \chi(r) \chi(r + \Delta\rho) \rangle \\ &= 4\pi^2 k^2 \int_0^H dz \sin^2 \left(\frac{z\kappa^2}{2k} \right) \int_0^\infty d\kappa \kappa \Phi_n(\kappa) J_0(\kappa \Delta\rho) \\ &= 4\pi^2 k^2 \int_0^H dz \sin^2 \left(\frac{z\kappa^2}{2k} \right) \int_0^\infty d\kappa \kappa \Phi_n(\kappa) J_0(\kappa v_\perp \tau) \\ &= 4\pi^2 H k^2 \int_0^\infty d\kappa \kappa \Phi_n(\kappa) J_0(\kappa v_\perp \tau) F_\chi(\kappa) \end{aligned} \quad (5)$$

where k is the radio signal's wave number, z is the turbulent layer length, κ is the turbulence spectrum wave number, and $\Phi_n(\kappa)$ is the turbulence spectrum function. For a slab model of the turbulence profile, we have

$$F_\chi(\kappa) = \frac{1}{2} \left[1 - \frac{\sin(H\kappa^2/k)}{H\kappa^2/k} \right] \quad (6)$$

The path integration is performed for a uniform atmosphere with thickness H .

Because the Bessel function $J_0(\kappa v_\perp \tau)$ is an even function, from Eqs. (1), (4), and (5) the power spectrum can be written as

$$W_\chi(\omega) = 8\pi^2 H k^2 \int_0^\infty d\kappa \kappa \Phi_n(\kappa) F_\chi(\kappa) \int_0^\infty J_0(\kappa v_\perp \tau) \cos(\tau\omega) d\tau \quad (7)$$

Using the result from the integration table,

$$\int_0^\infty J_\nu(ax) \cos(bx) dx = \begin{cases} \cos[\nu \sin^{-1}(b/a)] / \sqrt{a^2 - b^2} & \text{for } 0 < b < a \\ -a^\nu \sin(\nu\pi/2) [b + \sqrt{b^2 - a^2}]^{-\nu} / \sqrt{b^2 - a^2} & \text{for } 0 < a < b, \nu > -1 \end{cases} \quad (8)$$

for $\nu = 0$, $a = \kappa v_\perp$, and $b = \omega$, we have

$$\int_0^\infty J_0(\kappa v_\perp \tau) \cos(\tau\omega) d\tau = \begin{cases} (\kappa^2 v_\perp^2 - \omega^2)^{-(1/2)} & \omega < \kappa v_\perp < \infty \\ 0 & 0 < \kappa v_\perp < \omega \end{cases} \quad (9)$$

so that after using v to replace v_\perp the power spectrum becomes

$$W_\chi(\omega) = 8\pi^2 H k^2 \int_{\omega/v}^\infty d\kappa \kappa \Phi_n(\kappa) \frac{F_\chi(\kappa)}{\sqrt{\kappa^2 v^2 - \omega^2}} \quad (10)$$

III. Power Spectrum for a Point Receiver

Using Eq. (10) and the Kolmogorov turbulent spectrum to describe the small eddies in the inertial range,

$$\Phi_n(\kappa, z) = 0.033 C_n^2(z) \kappa^{-(11/3)}, \quad 0 < \kappa < \infty \quad (11)$$

(where C_n^2 is the refractive-index structure constant) gives the following for a point receiver:

$$W_\chi(\omega) = 1.303 H k^2 C_n^2 \int_{\omega/v}^\infty \frac{d\kappa}{\kappa^{8/3} \sqrt{\kappa^2 v^2 - \omega^2}} \left[1 - \frac{\sin(\kappa^2 H/k)}{\kappa^2 H/k} \right] \quad (12)$$

The first integration can be performed as

$$\mathcal{J}_1 = \int_{\omega/v}^{\infty} \frac{d\kappa}{\kappa^{8/3} \sqrt{\kappa^2 v^2 - \omega^2}} = 0.841 \frac{v^{5/3}}{\omega^{8/3}} \quad (13)$$

The second integration is found, after substituting $u = (\kappa v / \omega)^2$, to be

$$\begin{aligned} \mathcal{J}_2 &= \int_{\omega/v}^{\infty} \frac{d\kappa}{\kappa^{8/3} \sqrt{\kappa^2 v^2 - \omega^2}} \left(\frac{\sin(\kappa^2 H/k)}{\kappa^2 H/k} \right) \\ &= \frac{kv^{11/3}}{2H\omega^{14/3}} \mathcal{I}_m \left[\int_1^{\infty} \frac{du}{u^{17/6} \sqrt{u-1}} \exp \left(i \frac{\omega^2 H}{kv^2} u \right) \right] \end{aligned} \quad (14)$$

where \mathcal{I}_m denotes the imaginary part of the bracketed function. Using the solution of the second type of Kummer function (confluent hypergeometric function), $U(a, b, z)$, shown in the Appendix,

$$\int_1^{\infty} e^{-zx} x^{b-a-1} (x-1)^{a-1} dx = e^{-z} \Gamma(a) U(a, b, z) \quad (15)$$

we have

$$\mathcal{J}_2 = \frac{kv^{11/3}}{2H\omega^{14/3}} \mathcal{I}_m \left[\exp \left(i \frac{\omega^2 H}{kv^2} \right) \Gamma \left(\frac{1}{2} \right) U \left(\frac{1}{2}, -\frac{4}{3}, i \frac{\omega^2 H}{kv^2} \right) \right] \quad (16)$$

We define the Fresnel frequency by the ratio of the cross-path wind velocity, v , over the Fresnel length, f_L :

$$\omega_0 = \frac{v}{f_L} = v \sqrt{\frac{k}{H}} = v \sqrt{\frac{2\pi}{\lambda H}} \quad (17)$$

The Fresnel frequency, ω_0 , is the most important parameter in governing the scintillation fluctuations, because only the eddies with Fresnel length f_L are efficient in generating amplitude scintillations. Thus,

$$\mathcal{J}_2 = 0.5 \frac{v^{5/3}}{\omega^{8/3}} \frac{\omega_0^2}{\omega^2} \mathcal{I}_m \left[\exp \left(i \frac{\omega^2 H}{kv^2} \right) \Gamma \left(\frac{1}{2} \right) U \left(\frac{1}{2}, -\frac{4}{3}, i \frac{\omega^2}{\omega_0^2} \right) \right] \quad (18)$$

The final power spectrum for a plane wave is

$$W_\chi(\omega) = 1.096 \frac{HC_n^2 k^2 v^{5/3}}{\omega^{8/3}} \left\{ 1 - \frac{0.594 \omega_0^2}{\omega^2} \mathcal{I}_m \left[\exp \left(i \frac{\omega^2}{\omega_0^2} \right) \Gamma \left(\frac{1}{2} \right) U \left(\frac{1}{2}, -\frac{4}{3}, i \frac{\omega^2}{\omega_0^2} \right) \right] \right\} \quad (19)$$

For a high-frequency approximation ($\omega \gg \omega_0$), we can ignore the Kummer function because of the term $(\omega_0/\omega)^2$ and find that

$$W_\chi^\infty(\omega) = 1.096 \frac{HC_n^2 k^2 v^{5/3}}{\omega^{8/3}} \quad (\text{Np})^2/\text{Hz} \quad \text{for } \omega \gg \omega_0 \quad (20)$$

For a low-frequency approximation, we can assume $\omega = 0$ in Eq. (12):

$$W_\chi^0(\omega) = 1.303 H k^2 C_n^2 \frac{1}{v} \int_{\omega/v}^{\infty} \frac{d\kappa}{\kappa^{11/3}} \left[1 - \frac{\sin(\kappa^2 H/k)}{\kappa^2 H/k} \right] \quad (21)$$

If we substitute $\zeta = \kappa^2 H/k$, this becomes

$$W_\chi^0(\omega) = 0.6515 \frac{H^{7/3} k^{2/3} C_n^2}{v} \int_0^\infty \frac{dx}{\zeta^{7/3}} \left(1 - \frac{\sin \zeta}{\zeta} \right) \quad (22)$$

$$W_\chi^0(\omega) = 0.425 \frac{H^{7/3} k^{2/3} C_n^2}{v} \quad (\text{Np})^2/\text{Hz} \quad \text{for } \omega \rightarrow 0 \quad (23)$$

The power spectrum ratio between the high-frequency and zero-frequency limits is

$$\frac{W_\chi(\omega)}{W_\chi(0)} = 2.577 \left(\frac{\omega_0}{\omega} \right)^{8/3} \left\{ 1 - 0.594 \frac{\omega_0^2}{\omega^2} \mathcal{I}_m \left[\exp \left(i \frac{\omega^2}{\omega_0^2} \right) \Gamma \left(\frac{1}{2} \right) U \left(\frac{1}{2}, -\frac{4}{3}, i \frac{\omega^2}{\omega_0^2} \right) \right] \right\} \quad (24)$$

IV. Corner Frequency

The corner frequency is another important parameter for the power spectrum, because it determines the shape of the spectrum of the amplitude scintillation. We define the corner frequency, ω_c , as the intersection between the asymptotes for high frequency and low frequency [3,5,6]. That is,

$$W_\chi^\infty(\omega_c) = W_\chi^0(\omega_c) \quad \text{at } \omega = \omega_c \quad (25)$$

For a point receiver and a slab model of the turbulence strength profile, after removing the second term in Eq. (24) when $\omega \rightarrow \infty$, we have

$$\omega_c = (2.577)^{3/8} \omega_0 = 1.426 \omega_0 \quad (26)$$

For a thin-layer model, $W_\chi^\infty(\omega)$ is the same as that for a slab model, because the high-frequency approximation removes the second term related to

$$F_\chi(\kappa) = \frac{1}{2} [1 - \cos(H\kappa^2/k)]$$

However, $W_\chi^0(\omega)$ is different from that for a slab model. Through an integration process similar to what we used to derive the amplitude variances for three turbulent models in [4], we have

$$W_\chi^0(\omega) = 0.992 \frac{H^{7/3} k^{2/3} C_n^2}{v} \quad (\text{Np})^2/\text{Hz} \quad \text{for } \omega \rightarrow 0 \quad (27)$$

Thus, we have

$$\omega_c = 1.04 \omega_0 \quad \text{for a thin layer} \quad (28)$$

For an exponential model,

$$F_\chi(\kappa) = \frac{1}{2} \left[\frac{(H\kappa^2/k)^2}{1 + (H\kappa^2/k)^2} \right]$$

For this model, $W_\chi^\infty(\omega)$ also does not change, but its low-frequency spectrum is

$$W_\chi^0(\omega) = 1.182 \frac{H^{7/3} k^{2/3} C_n^2}{v} \quad (\text{Np})^2/\text{Hz} \quad \text{for } \omega \rightarrow 0 \quad (29)$$

Thus, the corner frequency is

$$\omega_c = 0.972 \omega_0 \quad \text{for an exponential profile} \quad (30)$$

The corner frequency for a finite-aperture antenna has a much complicated feature, which will be studied in Section VI.

V. Power Spectrum for a Large Antenna

A. Spatial Covariance

From the study in [4], we know that there is an aperture-smoothing (or -averaging) effect on the amplitude variance for a parabolic reflector. One would expect a similar effect for the spatial covariance. After integrating over the entire antenna surface with an aperture effective radius of a_r , a term $[2J_1(\kappa a_r)/\kappa a_r]^2$ is included. The aperture-averaged amplitude variance becomes

$$\begin{aligned} \overline{\langle \chi_1 \chi_2 \rangle} &= 4\pi^2 k^2 \int_0^\infty \kappa d\kappa \int_0^H dz \Phi_n(\kappa, z) \sin^2\left(\frac{z\kappa^2}{2k}\right) \left[\frac{2J_1(\kappa a_r)}{\kappa a_r} \right]^2 \\ &= 2\pi^2 k^2 \int_0^\infty \kappa d\kappa \Phi_n(\kappa, z) \left[1 - \frac{\sin(\kappa^2 H/k)}{\kappa^2 H/k} \right] \left[\frac{2J_1(\kappa a_r)}{\kappa a_r} \right]^2 \end{aligned} \quad (31)$$

Actually, this averaging process on the antenna aperture is equivalent to a convolution of the spectral fluctuations with a two-dimensional antenna surface [3,7].

For the spatial covariance, there is an additional term, $J_0(\kappa\rho)$, due to the inter-receiver correlation $\rho = v_\perp \tau$, as shown in Eq. (5). This is also sometimes called the Hankel transform with a weighted function of $J_0(\kappa\rho)[2J_1(\kappa a_r)/\kappa a]^2$:

$$B_\chi(\rho, a_r) = 2\pi^2 k^2 \int_0^\infty \kappa d\kappa \Phi_n(\kappa, z) \left[1 - \frac{\sin(\kappa^2 H/k)}{\kappa^2 H/k} \right] J_0(\kappa\rho) \left[\frac{2J_1(\kappa a_r)}{\kappa a_r} \right]^2 \quad (32)$$

For the sake of simplification, we have used a slab profile model for the calculation here. Using the Fourier transform relations shown in Eqs. (1) and (10), the aperture-averaged power spectrum for a finite-aperture antenna becomes

$$W_{\bar{\chi}}(\omega, a_r) = 4\pi^2 H k^2 \int_{\omega/v}^{\infty} d\kappa \kappa \Phi_n(\kappa) \frac{1}{\sqrt{\kappa^2 v_{\perp}^2 - \omega^2}} \left[1 - \frac{\sin(\kappa^2 H/k)}{\kappa^2 H/k} \right] \left[\frac{2J_1(\kappa a_r)}{\kappa a_r} \right]^2 \quad (33)$$

B. Airy Functions and Aperture Smoothing

The term $[2J_1(\kappa a_r)/\kappa a_r]^2$ in Eq. (33) is called the Airy function. It acts as a lowpass filter to remove all frequency components higher than the aperture-smoothing frequency that will be defined later. In order to solve the above integral, we approximate the Airy function by a Gaussian pattern [3]:

$$[2J_1(\kappa a_r)/\kappa a_r]^2 \approx \exp(-b^2 \kappa^2 a_r^2)$$

For a best fit, we use $b = 0.4832$ as shown in Fig. 1. Thus, the Gaussian term plays an antenna cutoff role with a turbulence wave number cutoff $\kappa_c = 1/ba_r$.

Inserting this approximation into Eq. (33), the integral becomes

$$W_{\bar{\chi}}(\omega, a_r) = 4\pi^2 H k^2 \int_{\omega/v}^{\infty} d\kappa \kappa \Phi_n(\kappa) \frac{1}{\sqrt{\kappa^2 v_{\perp}^2 - \omega^2}} \left[1 - \frac{\sin(\kappa^2 H/k)}{\kappa^2 H/k} \right] \exp(-b^2 \kappa^2 a_r^2) \quad (34)$$

Here we need to define a new frequency called the aperture-smoothing frequency, $\omega_s = v/ba_r$, which is defined as wind speed over the entire antenna aperture. The frequency is related to the Fresnel frequency by $\omega_s = \omega_0/\gamma$, where

$$\gamma = ba_r \sqrt{k/H} \propto \frac{a_r}{f_L}$$

which is a ratio between the antenna radius and the largest size of the Fresnel zone. The ratio of ω_s/ω_0 as a function of actual antenna radius is shown in Fig. 2, where we have assumed a 55 percent antenna radius efficiency. That is, $a_r = 55\% \times$ the actual antenna radius. For a DSN 34-m-diameter receiver (the radius = 17 m), we have $\omega_s/\omega_0 = 0.79$, as shown in Fig. 2. The aperture-smoothing effects will depend primarily upon this ratio. We can see that an antenna with a finite aperture imposes a high wave-number cutoff on the spectrum of the refractivity fluctuations (similar to a lowpass filter). Averaging effects become significant when the transverse correlation length of the scintillation is smaller than the antenna radius. Incident wave-front fluctuations are averaged out by a large aperture. Thus, the wave fluctuations appear uncorrelated with this type of receiver.

Using substitutions of $t = \kappa^2 v_{\perp}^2 / \omega^2 - 1$ and $\sin(\kappa^2 H/k) = \mathcal{I}_m [\exp(i\kappa^2 H/k)]$, definitions of ω_0 and ω_s , and applying the Kolmogorov spectrum, we have

$$W_{\bar{\chi}}(\omega, a_r) = 0.6515 H k^2 C_n^2 v^{5/3} \omega^{-(8/3)} \left\{ \begin{array}{l} \int_0^{\infty} (t+1)^{-(11/6)} t^{-(1/2)} \exp\left(-\frac{\omega^2}{\omega_s^2} t\right) \exp\left(-\frac{\omega^2}{\omega_s^2}\right) dt \\ - \left(\frac{\omega_0}{\omega}\right)^2 \mathcal{I}_m \left[\int_0^{\infty} (t+1)^{-(17/6)} t^{-(1/2)} \exp\left(-\frac{\omega^2}{\omega_s^2} t - \frac{\omega^2}{\omega_s^2}\right) \right. \\ \left. \exp\left(i\frac{\omega^2}{\omega_0^2} t + i\frac{\omega^2}{\omega_0^2}\right) dt \right] \end{array} \right\} \quad (35)$$

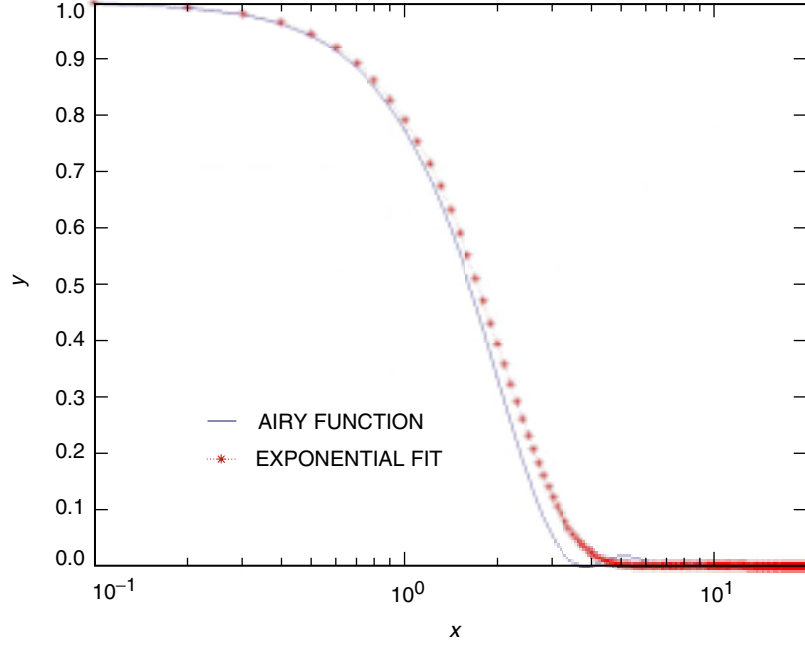


Fig. 1. Using a Gaussian function to fit the Airy function. The best fit coefficient is $b = 0.4832$, where $x = \kappa a_r$, while y shows values of both functions.

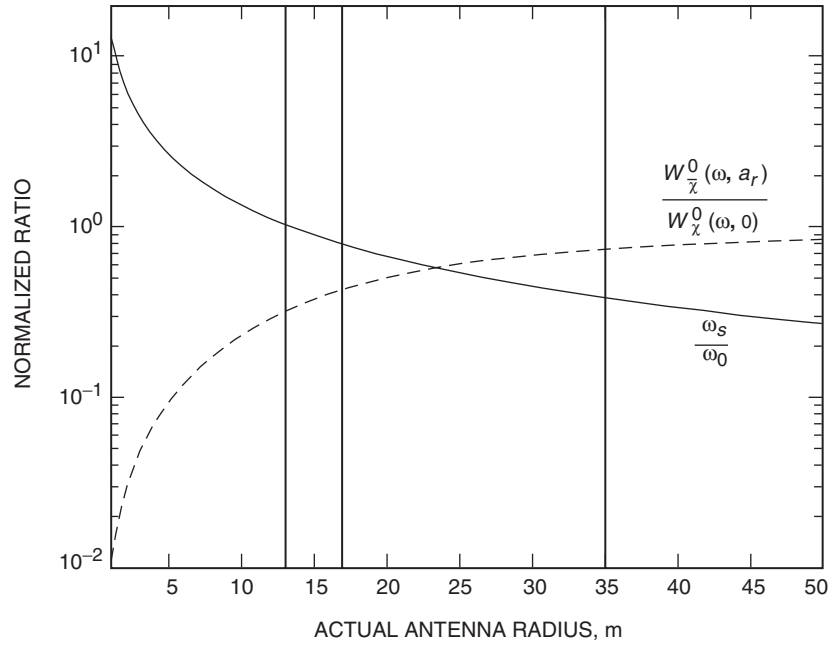


Fig. 2. The ratio of ω_s/ω_0 as a function of actual antenna radius (physical radius). A normalized low-frequency approximation of $W_{\chi}^0(\omega, a_r)/W_{\chi}^0(\omega, 0)$ is also shown. Vertical lines at radii of 13 m, 17 m, and 35 m show cross-values for two curves, respectively.

Using another solution of the Kummer function (the confluent hypergeometric function) described in the Appendix,

$$\int_0^\infty x^{a-1}(1+x)^{b-a-1}e^{-zx}dx = \Gamma(a)U(a, b, z) \quad (36)$$

the power spectrum solution for a finite-aperture receiver becomes

$$W_{\bar{\chi}}(\omega, a_r) = 0.6515Hk^2C_n^2v^{5/3}\omega^{-(8/3)} \left\{ \begin{array}{l} \left[\Gamma\left(\frac{1}{2}\right) U\left(\frac{1}{2}, -\frac{1}{3}, \frac{\omega^2}{\omega_s^2}\right) \exp\left(-\frac{\omega^2}{\omega_s^2}\right) \right] \\ - \left(\frac{\omega_0}{\omega}\right)^2 \mathcal{I}_m \left[\Gamma\left(\frac{1}{2}\right) U\left(\frac{1}{2}, -\frac{4}{3}, \frac{\omega^2}{\omega_s^2} - i\frac{\omega^2}{\omega_0^2}\right) \right] \\ \exp\left(i\frac{\omega^2}{\omega_0^2} - \frac{\omega^2}{\omega_s^2}\right) \end{array} \right\} \quad (37)$$

C. Low- and High-Frequency Approximations

We will study two cases: $\omega = 0$ (low-frequency approximation) and $\omega = \infty$ (high-frequency approximation) for $a_r \neq 0$ (a finite-aperture antenna). In the previous section, we studied both cases for a point receiver when $a_r = 0$. Here we will study the case when $a_r \neq 0$ (including a DSN large-diameter antenna).

When $\omega \rightarrow \infty$, the power spectrum in the second term of Eq. (37) in brackets becomes so small that it can be neglected, due to the factor $(\omega_0/\omega)^2$. Thus, for the high-frequency approximation, we have

$$\begin{aligned} W_{\bar{\chi}}^\infty(\omega, a_r) &= 0.6515Hk^2C_n^2v^{5/3}\omega^{-(8/3)} \left[\Gamma\left(\frac{1}{2}\right) U\left(\frac{1}{2}, -\frac{1}{3}, \frac{\omega^2}{\omega_s^2}\right) \exp\left(-\frac{\omega^2}{\omega_s^2}\right) \right] \\ &= 1.1548Hk^2C_n^2v^{5/3}\omega^{-(8/3)} \left(\frac{\omega_s}{\omega}\right) \exp\left(-\frac{\omega^2}{\omega_s^2}\right) \end{aligned} \quad (38)$$

because $\Gamma(1/2) = \sqrt{\pi}$, and $U[(1/2), -(1/3), (\omega^2/\omega_s^2)] = \omega_s/\omega$, when $\omega \rightarrow \infty$.

Thus, the normalized ratio of the power spectrum for a finite-aperture receiver relative to that for a point receiver in Eq. (20) is given by

$$\frac{W_{\bar{\chi}}^\infty(\omega, a_r)}{W_{\chi}^\infty(\omega, 0)} = 1.053 \left(\frac{\omega_s}{\omega}\right) \exp\left(-\frac{\omega^2}{\omega_s^2}\right) \quad (39)$$

This ratio shows that above the aperture-smoothing frequency, ω_s , the spectrum is rolling off but no longer at a rate of $\omega^{-(8/3)}$, which characterizes a point receiver in Eq. (20). Instead, it damps at a much faster rate of $\exp(-\omega^2/\omega_s^2)$. The power spectral density for $W_{\bar{\chi}}^\infty(\omega, \omega_s)$ (as a case for $\omega \rightarrow \infty$) is plotted in Fig. 3 for a case of $\omega_s = 0.79\omega_0$ (corresponding to a 34-m-diameter antenna). As a comparison, we also plot it in Fig. 4 for a case of $\omega_s = 1.0\omega_0$, corresponding to an actual 26-m-diameter antenna.

The normalized power spectra are plotted in Figs. 5 and 6 for both antenna radii. We can see that the Fourier components with frequencies greater than ω_s are damped at a rate of $\exp(-\omega^2/\omega_s^2)$ due to

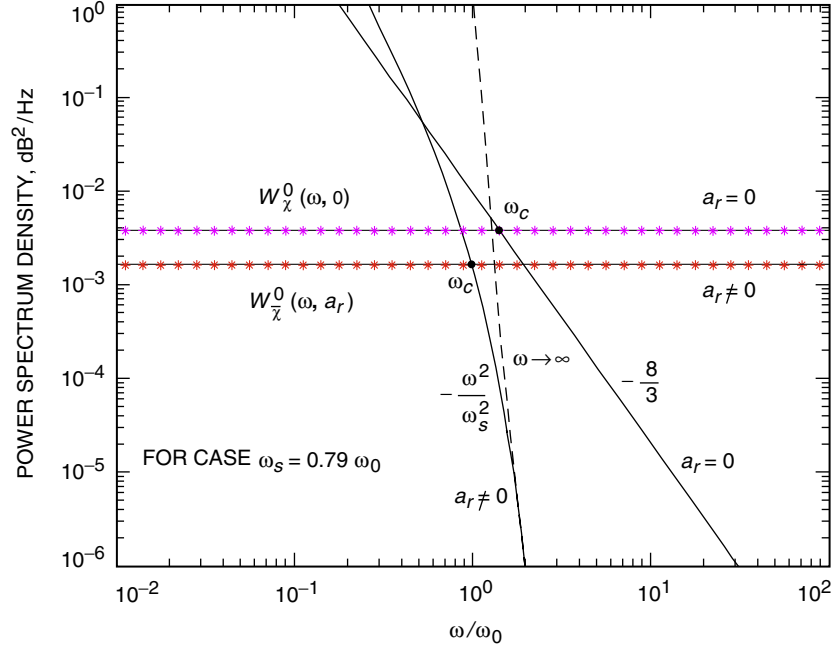


Fig. 3. Power spectrum density (dB^2/Hz) as a function of ω/ω_0 for a case of $\omega_s = 0.79\omega_0$ (for a DSN 34-m-diameter antenna).

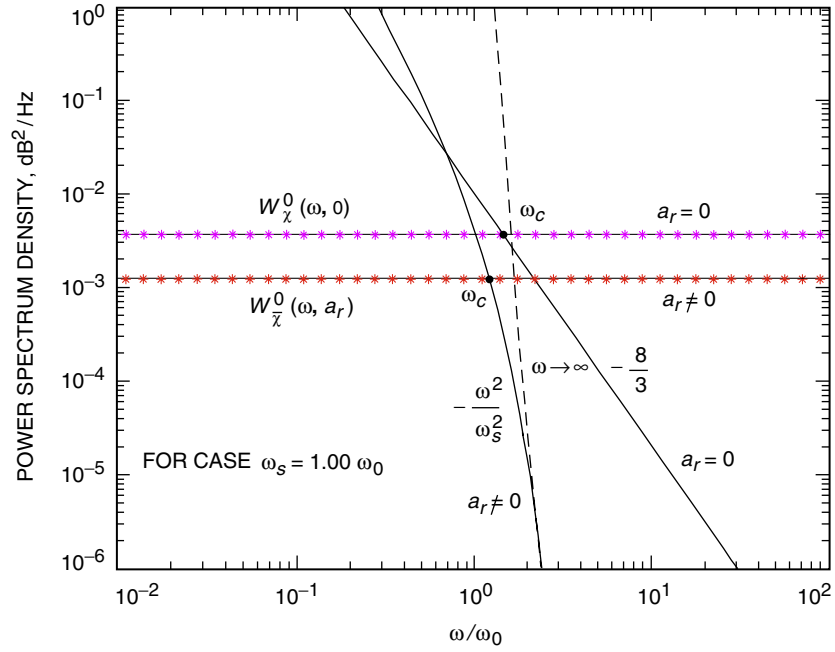


Fig. 4. Power spectrum density (dB^2/Hz) as a function of ω/ω_0 for a case of $\omega_s = 1.0 \omega_0$ (for a 26-m-diameter antenna).

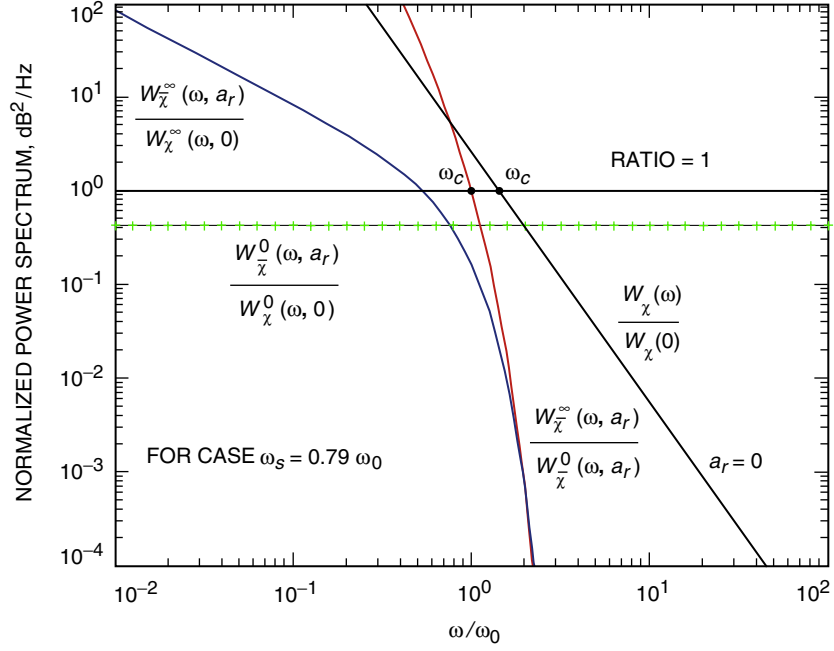


Fig. 5. Normalized power spectrum density as a function of ω/ω_0 for a case of $\omega_s = 0.79\omega_0$ (for a DSN 34-m-diameter antenna).

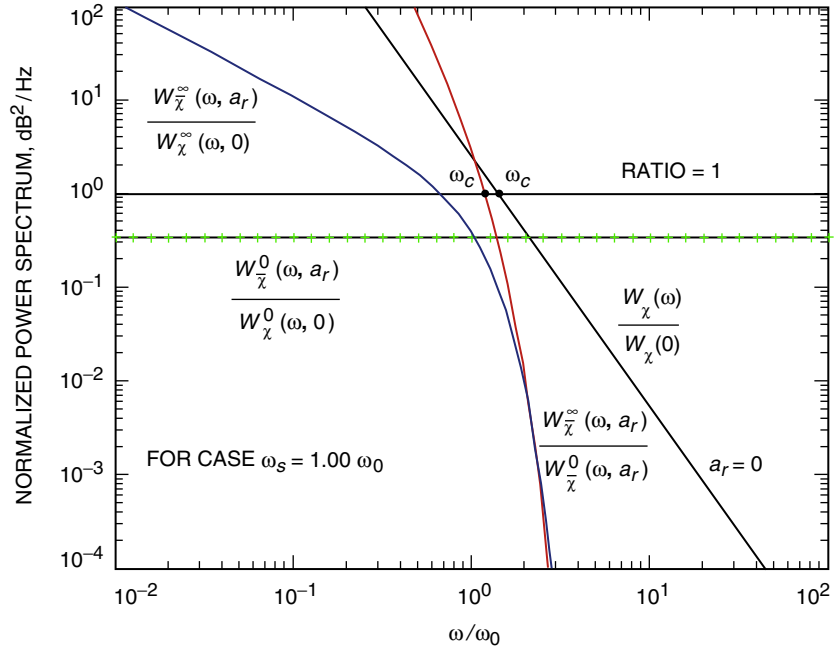


Fig. 6. Normalized power spectrum density as a function of ω/ω_0 for a case of $\omega_s = 1.0 \omega_0$ (for a 26-m-diameter antenna).

aperture-smoothing effects. This is much faster than the rate of $f^{-(8/3)}$ for a point antenna. All spectral power values are reduced relative to a point receiver. The smoothing effects become more significant when ω_s becomes smaller, that is, a larger antenna a_r , and a larger ratio γ , or a smaller velocity v .

When $\omega \rightarrow 0$, for a low-frequency approximation we have

$$W_\chi^0(\omega) = 1.303 H k^2 C_n^2 v^{-1} \int_{\omega/v}^{\infty} \frac{d\kappa}{\kappa^{11/3}} \left[1 - \frac{\sin(\kappa^2 H/k)}{\kappa^2 H/k} \right] \exp(-b^2 \kappa^2 a_r^2) \quad (40)$$

After a substitution of $t = \kappa^2 H/k$, we have

$$W_\chi^0(\omega) = 0.6515 H^{7/3} k^{2/3} C_n^2 v^{-1} \int_0^\infty \left\{ \begin{array}{c} t^{-(7/3)} \exp\left(-\frac{\omega_s^2}{\omega_0^2} t\right) \\ - \mathcal{I}_m \left[t^{-(10/3)} \exp\left(-\frac{\omega_s^2}{\omega_0^2} t + it\right) \right] \end{array} \right\} dt \quad (41)$$

Using the standard integral result,

$$\int_0^\infty t^{a-1} \exp(-\beta t) dt = \Gamma(a) \beta^{-a} \quad (42)$$

we have

$$W_{\bar{\chi}}^0(\omega, a_r) = 0.6515 H^{7/3} k^{2/3} C_n^2 v^{-1} \left\{ \Gamma\left(-\frac{4}{3}\right) \left(\frac{\omega_s^2}{\omega_0^2}\right)^{4/3} - \mathcal{I}_m \left[\Gamma\left(-\frac{7}{3}\right) \left(\frac{\omega_s^2}{\omega_0^2} - i\right)^{7/3} \right] \right\} \quad (43)$$

Normalizing by a point receiver spectrum, Eq. (23), we have

$$\frac{W_{\bar{\chi}}^0(\omega, a_r)}{W_\chi^0(\omega, 0)} = 1.533 \left\{ \Gamma\left(-\frac{4}{3}\right) \left(\frac{\omega_s^2}{\omega_0^2}\right)^{4/3} - \mathcal{I}_m \left[\Gamma\left(-\frac{7}{3}\right) \left(\frac{\omega_s^2}{\omega_0^2} - i\right)^{7/3} \right] \right\} \quad (44)$$

which is a function of only ω_s and ω_0 . We have plotted this ratio in Fig. 2 as a function of actual antenna radius. When the radius is 17 m, the ratio is 0.43.

In Fig. 3, we have plotted absolute power spectral density (in dB²/Hz) calculated from power spectrum equations for a case of $\omega_s = 0.79\omega_0$, corresponding to an actual 17-m aperture radius. There are two spectral lines plotted for a point receiver ($a_r = 0$). One is the high-frequency approximation, $W_\chi^\infty(\omega, 0)$, from Eq. (20), which is falling off at a rate of $-(8/3)$ on a loglog plot. Another one is the low-frequency approximation, $W_\chi^0(\omega, 0)$, from Eq. (23), a straight horizontal line, which is independent of ω with a constant value of about 0.004 dB²/Hz. Power spectral lines for a finite-aperture also are plotted. While the straight horizontal line marked with $W_{\bar{\chi}}^0(\omega, a_r)$ at about 0.002 dB²/Hz is its low-frequency approximation from Eq. (38), the line marked with $-\omega^2/\omega_s^2$ is its high-frequency approximation, $W_{\bar{\chi}}^\infty(\omega, a_r)$, from Eq. (38). In addition, a straight line as an asymptote from Eq. (37) also is drawn, with a mark of $\omega \rightarrow \infty$. We can see that apparent differences in the high-frequency spectra between a point and a finite-aperture receiver are that the latter has a much faster damping rate than does the former, and it filters out more fluctuated power.

We also have made a similar plot in Fig. 4 for the $\omega_s = 1.0\omega_0$ case, corresponding to a 13-m-aperture radius. Compared with Fig. 3, we can see that $W_{\bar{\chi}}^{\infty}(\omega, a_r)$ shifts to the higher frequency, but with a smaller damping rate because of the larger ω_s . $W_{\bar{\chi}}^0(\omega, a_r)$ goes to 0.0012 dB²/Hz as ω_s increases. The point receiver spectral solutions are still the same because they are independent of ω_s .

In Figs. 5 and 6, the normalized power spectra are plotted for both types of receivers ($a_r = 0$ and $a_r \neq 0$). While Fig. 5 shows a case of $\omega_s = 0.79\omega_0$, Fig. 6 is for $\omega_s = 1.0\omega_0$. For a point receiver spectrum ($a_r = 0$), we have normalized a high-frequency approximation by its low-frequency solution, $W_{\chi}(\omega)/W_{\chi}(0)$, as shown in Eq. (24). The straight line has a $-8/3$ slope in a loglog scale.

For a finite-aperture receiver, we first normalize the high-frequency solution by a high-frequency solution for a point receiver, $W_{\bar{\chi}}^{\infty}(\omega, a_r)/W_{\chi}^{\infty}(\omega, 0)$, that is, normalized by its antenna aperture, as shown in Eq. (39). This ratio defines the aperture-smoothing effects. Then we normalize the high-frequency solution by its low-frequency version: $W_{\bar{\chi}}^{\infty}(\omega, a_r)/W_{\bar{\chi}}^0(\omega, a_r)$. As we will see in the next section, this cross-normalization ratio will define the corner frequency. We see that both normalized ratios decrease rapidly with increasing frequency at a rate of $\exp(-\omega^2/\omega_s^2)$ when $\omega > \omega_s$. Lastly, we normalize the low-frequency finite-aperture solution by a low-frequency point receiver solution, $W_{\bar{\chi}}^0(\omega, a_r)/W_{\chi}^0(\omega, 0)$, as shown in Eq. (44). This is always less than unity, because the power spectrum for a finite-aperture receiver is always less than that for a point receiver. In Fig. 5 this ratio is 0.43, and in Fig. 6 this ratio is 0.33, because $W_{\bar{\chi}}^0(\omega, a_r)$ decreases with increasing ω_s , while $W_{\chi}^0(\omega, 0)$ does not. We also have plotted a line with ratio = 1.0 in both figures for reference. The four plots in Figs. 3 through 6 will define the shapes of the power spectra for a finite-aperture receiver, because the more important corner frequencies can be determined from these plots, as we will see in the next section.

VI. Corner Frequency for a Finite-Aperture Antenna

To calculate the corner frequency for a finite-aperture antenna, we need to calculate the ratio between power spectra given in Eqs. (38) and (43) [3,6]:

$$\begin{aligned} \frac{W_{\bar{\chi}}^{\infty}(\omega, a_r)}{W_{\bar{\chi}}^0(\omega, a_r)} &= 1.773 \left(\frac{\omega_0}{\omega}\right)^{8/3} \left(\frac{\omega_s}{\omega}\right) \exp\left(-\frac{\omega^2}{\omega_s^2}\right) \\ &\times \left\{ \Gamma\left(-\frac{4}{3}\right) \left(\frac{\omega_s^2}{\omega_0^2}\right)^{4/3} - \mathcal{I}_m \left[\Gamma\left(-\frac{7}{3}\right) \left(\frac{\omega_s^2}{\omega_0^2} - i\right)^{7/3} \right] \right\}^{-1} \end{aligned} \quad (45)$$

We can solve for the corner frequency by setting $W_{\bar{\chi}}^{\infty}(\omega, a_r) = W_{\bar{\chi}}^0(\omega, a_r)$. The corner frequency cannot be solved analytically from Eq. (45). However, we can find these values from the graphic intersections shown in Figs. 3 through 6.

As we know, the corner frequency is defined as the intersection between the high-frequency asymptote and low-frequency asymptote. We can see that in Fig. 3, which shows the absolute value of the power spectrum, this intersection value for a point receiver is $\omega_c = 1.43\omega_0$, while $\omega_c = 1.0\omega_0$ for a finite-aperture receiver with a 17-m actual antenna radius. In Fig. 4, the corner frequency for a point receiver does not change, but for a receiver with a 13-m actual antenna radius, the corner frequency increases to $1.15\omega_0$.

In Figs. 5 and 6 (normalized power spectrum), the corner frequencies are values intersected with a line of the ratio = 1, as shown in Eq. (24) for a point receiver and Eq. (45) for a finite-aperture receiver. We have shown this horizontal line in both figures. We can see that in Fig. 5 (17-m-radius antenna case) $W_{\chi}(\omega)/W_{\chi}(0)$ intersects the line at $\omega_c = 1.43\omega_0$ as expected, while $W_{\bar{\chi}}^{\infty}(\omega, a_r)/W_{\bar{\chi}}^0(\omega, a_r)$ has a cross-value with the line at $\omega_c = 1.0\omega_0$. These results are exactly the same as those we obtained from

Fig. 3. Figure 6 also shows the same solution as that in Fig. 4 for a case of $\omega_s = 1.0\omega_0$. The corner frequency is $1.15\omega_0$ for a receiver with a 13-m actual aperture radius, increasing as the curve shifts to the higher frequency. We have marked out all corner frequencies (ω_c) in the four figures using dots. Thus, we can see that from two types of graphics (normalized and unnormalized power spectra), we have obtained the same graphic solutions for the corner frequency.

Using the above method, we have found all graphic solutions of the corner frequency ω_c for various ω_s . We have plotted a normalized corner frequency ω_c/ω_0 as a function of ω_s/ω_0 in Fig. 7. A straight line is used to fit these corner frequency values marked by the crosses. It is seen that ω_c almost linearly increases with increasing ω_s (decreasing antenna size) for a finite-aperture receiver. Three horizontal lines show the corner frequency values respective to three types of turbulence models for a point receiver. When we also apply a slab turbulence model to a finite-aperture antenna, its corner frequency value should not exceed the value $1.43\omega_0$ from a point receiver, even though Eq. (45) can have a larger solution than $1.43\omega_0$. Due to the aperture-smoothing effects, the spectrum for a finite-aperture receiver cannot have frequency components higher than those for a point receiver. Thus, we have used a dashed line to show the part of ω_c with values greater than $1.43\omega_0$ in Fig. 7, which corresponds to $1.35\omega_0$ for ω_s and a 6-m-radius antenna. Vertical dashed lines give the cases of two types of ω_s values applied for this study ($0.79\omega_0$ and $1.0\omega_0$).

VII. Application to the DSN Goldstone Receiver

We will use the following parameters for the power spectrum calculation for the Deep Space Network (DSN) Goldstone site [6,8]: $\lambda = 0.01$ (m) for 32-GHz (Ka-band); $H = 8.0 \times 10^3$ (m); $a_r = 34/2 \times 55\%$ (m); and $v = 10$ (m/s) for the wind speed.

Here we have assumed that the DSN 34-m-diameter antenna has a 55 percent efficient radius relative to its physical radius at Ka-band. These parameters have been used for the calculations in deter-

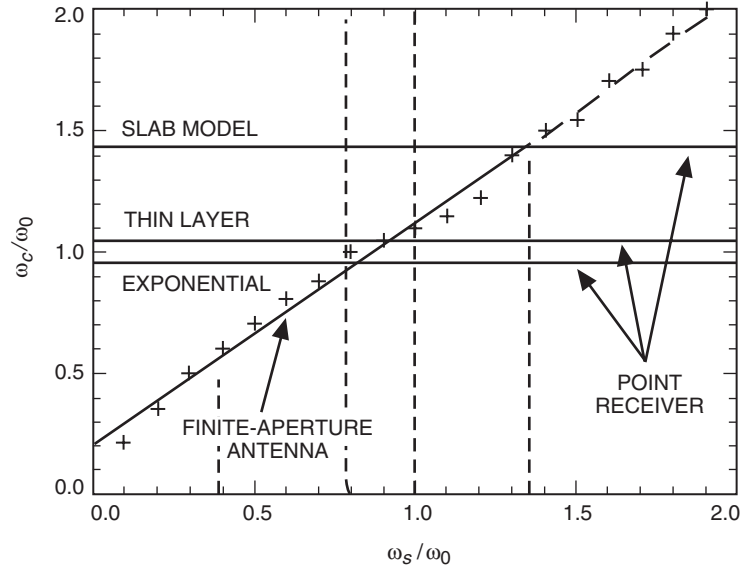


Fig. 7. Normalized corner frequency ω_c/ω_0 as a function of the ratio of ω_s/ω_0 . Corner frequency values (crosses), which can be fitted linearly, increase with increasing ω_s . When $\omega_s/\omega_0 > 1.35$, ω_c does not have a real solution, because the upper limit for a point receiver in ω_c is $1.43\omega_0$.

mining ω_0 , ω_s , and ω_c in previous sections. Thus, for a 34-m antenna we have the following: Fresnel frequency, $\omega_0 = v\sqrt{\lambda H/2\pi} = 2.8$ rad/s, $f_0 = 0.44$ Hz; aperture-smoothing frequency, $\omega_s = v/ba_r = 2.2$ rad/s, $f_s = 0.35$ Hz, and $\omega_s = 0.79\omega_0$; and corner frequency for a finite-aperture antenna, $\omega_c = 1.0\omega_0 = 2.8$ rad/s, $f_c = 0.44$ Hz.

If we define the fading rate (or fading slope) as $r_f = \chi_{\text{rms}} \cdot f_c$, where χ_{rms} is the maximum rms of the amplitude variance (or amplitude fluctuation in decibels) calculated in [4], we have the maximum fading rate as $r_f = 0.13 \text{ dB} \times 0.44 \text{ Hz} \approx 0.06 \text{ dB/s}$.

For a 26-m-diameter receiver, we have $\omega_s = 1.0\omega_0 = 2.8$ rad/s, $f_s = 0.44$ Hz (from Fig. 2), and $\omega_c = 1.15\omega_0 = 3.2$ rad/s, $f_c = 0.51$ Hz. For a 70-m-diameter receiver, we have $\omega_s = 0.38\omega_0 = 1.06$ rad/s (from Fig. 2) and $\omega_c = 0.57\omega_0 = 1.6$ rad/s, $f_c = 0.25$ Hz.

Based on the corner frequency and graphics of power spectrum solutions we obtained from the previous section, we can define the shape of the power spectrum of atmospheric scintillations for the DSN Goldstone 34-m receiver. We have drawn an expected spectrum for fast amplitude fluctuations in Fig. 8. Normalized power spectra versus normalized frequency are shown for both a point receiver and a finite-aperture receiver. Above their corner frequencies ($\omega_c = 1.43\omega_0$ for a point receiver, and $\omega_c = 1.0\omega_0$ for a 34-m-diameter receiver, respectively), the power damps at a rate of $f^{-(8/3)}$ for a point receiver, while it rolls off at a rate of $f^{-(\omega/\omega_s)^2}$ for a finite receiver. It should be pointed out that whether or not there is an obvious fast falling shape of the power spectrum for a finite-aperture receiver also depends much on the receiver's noise level. When the receiver has a relatively high noise floor as the DSN receiver has (as shown by a line in Fig. 8), the actual differences between the power spectra of a point receiver and a finite-aperture receiver are so small because the noise floor is very close to the scintillation peak power. The falling rates are not easily distinguished. However, we believe that the difference will become significant when the noise level is reduced.

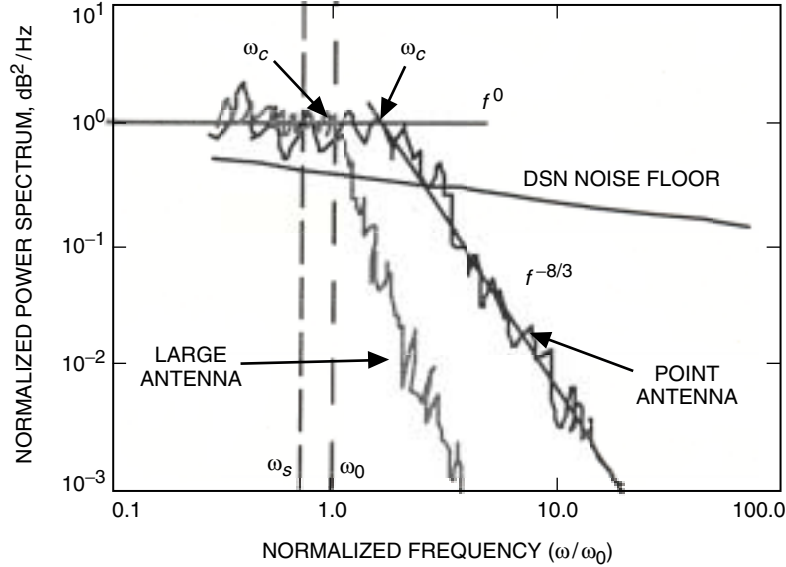


Fig. 8. A drawing shows the expected power spectrum shapes for a finite-aperture antenna and a point receiver. The DSN receiver's noise level is also drawn, which is so close to the peak scintillation power that the aperture smoothing effect is hard to identify.

VIII. Comparison with Experimental Studies

We can compare the above theoretical results with previous Ka-band experimental studies. The Advanced Communications Technology Satellite (ACTS) provided the first high time resolution (20 samples/s) measurements [9]. Figure 9 shows a power spectrum measured from ACTS [10]. The ACTS measurements were made at Norman, Oklahoma, on August 9, 1996, using a 1.2-m-diameter antenna, which can be regarded as a point receiver. The observation site has an elevation angle of 49.1 deg. The ACTS sent beacon signals at two frequencies: 20 GHz and 27 GHz. We can see the power at high frequencies falling off at a rate slower than the $-8/3$ power law.

Figure 10 is an example from the study of Cox et al. [11] showing antenna aperture-smoothing effects. Power spectra from Comstar beacon signals (28.56 GHz) were measured at Crawford Hill, New Jersey (an elevation angle of 41.5 deg), August 1–3, 1979, using a 7-m-diameter antenna. We can see that the power at high frequency falls off at a faster rate than the $-8/3$ power law for a point receiver. It is found that its damping rate is consistent with theoretical expectation for the aperture-averaging effects [3]. Furthermore, from our results as shown in Fig. 7, we predict that only when effective antenna radius $a_r \geq 6$ m (that is, $\omega_s/\omega_0 \leq 1.35$) can we start to see obvious aperture-smoothing effects due to the increase in the corner frequency. When $a_r \leq 6$ m, its corner frequency should not be any different from that for a point receiver.

IX. Summary

The power spectrum of fast-fluctuated signals can provide important information about variability in frequency range and power intensity. Using these parameters, we can determine the fading rate, which has a direct impact on Ka-band downlink availability for a very sensitive DSN receiving system. Through this study, we find that the temporal spectrum of amplitude scintillation is dependent on the frequency of microwave signals (or wavelength), wind speed, Fresnel length of the turbulent eddy zone, and antenna aperture. The Fresnel length, f_L , of eddies is the most efficient scale length in generating the amplitude scintillations. Aperture-averaging effects become significant when the transverse correlation length of the scintillation is smaller than the antenna radius. A finite aperture acts as a lowpass filter to filter out

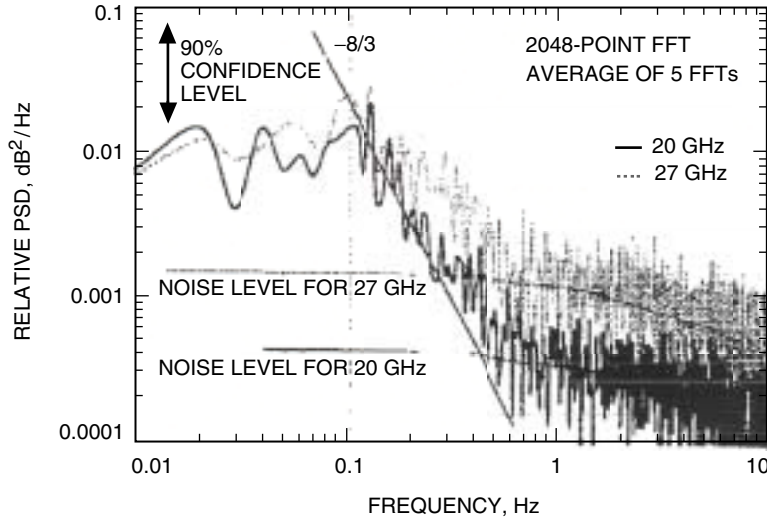


Fig. 9. A comparison with experimental measurements from ACTS at Oklahoma. The power spectrum generated from a 1.2-m receiver fits very well to a power law of $-8/3$ for a point receiver [10].

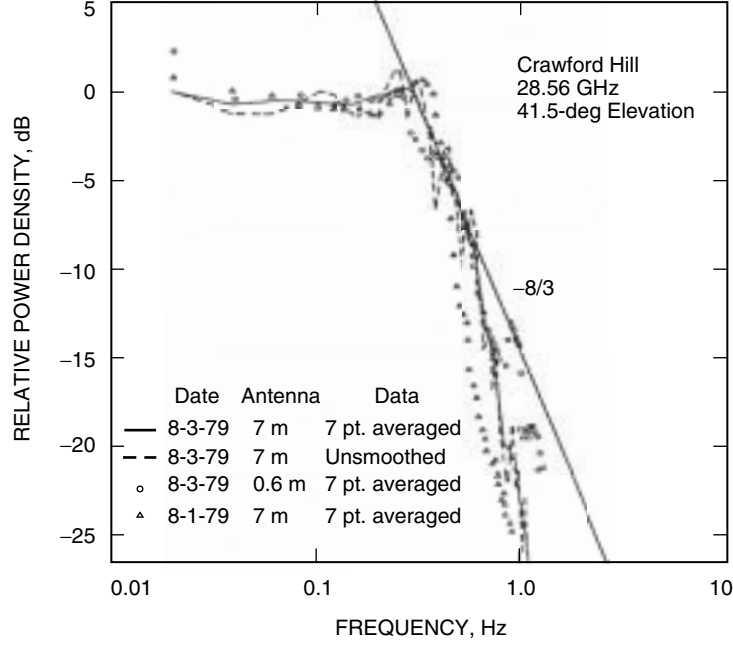


Fig. 10. A comparison with previous experiments from the COMSTAR satellite. Beacon signals were received by both the 0.6-m and 7-m antennas. A line with $-8/3$ power law basically fits measurements from the 0.6-m antenna (circles), while measurements from the 7-m antenna (triangles) depart from the straight line with a faster falling rate at higher frequencies [11].

all frequency components higher than the aperture-smoothing frequency. The power spectrum solution for a point receiver is expanded for a finite-aperture receiver through a two-dimensional antenna surface convolution. The Airy function as a key term in the spectral expression is approximated by a Gaussian pattern that imposes a high wave-number cutoff on the atmospheric turbulence spectrum. The aperture-smoothing frequency, ω_s , is fully studied as a function of antenna radius, while the corner frequency, ω_c , is solved through a detailed graphical analysis.

We find that, for frequencies that lie above the aperture-smoothing frequency ω_s , the spectrum rolls off at a much faster rate of $\exp(-\omega^2/\omega_s^2)$, instead of a rate of $\omega^{-(8/3)}$, as for a point receiver. The spectral density rolling off appears to be indicative of aperture smoothing at high-frequency Fourier components. We like to emphasize that the smoothing factor for the high-frequency approximation depends only on the ratio of wind speed to effective antenna size. We further note that whether or not aperture-smoothing effects are clearly seen in the power spectrum also depends on the receiver's noise floor.

An important frequency, the corner frequency, which is the turning (or break) point from low frequency to high frequency in the power spectrum, is defined for the spectral analysis. We have applied these solutions to the scenario of a DSN Goldstone 34-m antenna and predicted power spectrum shape for the receiving station. When the aperture-smoothing frequency is $0.79f_0$ (or 0.35 Hz), where $f_0 = 0.44$ Hz, the maximum corner frequency for the receiver is 0.44 Hz (or $1.0f_0$). The corner frequency increases with decreasing antenna size. When $a_r \leq 6$ m (actual radius = 11 m for a 55 percent efficiency), $\omega_c = 1.43\omega_0$, a corner frequency for a point receiver has been reached. Its corner frequency will not increase any more. The corresponding fading rate (or fading slope) is 0.06 dB/s for a 0.13-dB amplitude fluctuation (rms). These values may be reduced when the wind speed and the turbulent layer thickness are changed.

Now we understand that the upper frequency (the corner frequency) of amplitude scintillations for a point receiver and a slab model is $1.43\omega_0$, controlled only by the Fresnel frequency (the wind speed over the Fresnel length of turbulent eddies). The upper frequency for a finite-aperture receiver is controlled by both the Fresnel frequency and aperture-smoothing frequency. The larger aperture always suppresses the high-frequency components, with the result that the corner frequency is lower than that for a point receiver. For example, for a 70-m-diameter receiver, the upper frequency (corner frequency) in the spectrum is reduced to 0.25 Hz. These results can be used for DSN telecommunications system design, Ka-band experimental sample-rate selection, and extrapolation of the Ka-band fading models developed from ACTS experiments for use in a large-aperture receiving station.

The frequency ranges of the power spectrum also depend on what types of atmospheric turbulence layer models we chose. In this study, we have used a slab model of atmospheric turbulences and the Kolmogorov turbulence spectrum for a finite-aperture receiver. In actual measurements, the corner frequency is hard to determine accurately from the individual power spectrum, due to the noise. Some authors have tried to use the spectral measurements on the smoothing effects as a remote sensing tool to deduce the wind speed and atmospheric turbulence structures [6]. Because Ka-band signal scintillation is greatly affected by the atmospheric condition, by using both Fresnel and corner frequencies the turbulence layer structure or the wind velocity can be inferred.

Acknowledgments

We wish to thank the Program Manager, Julian Breidenthal, for his support in this propagation effects study. We also are indebted to Dave Morabito for his reviewing of this article and Bob Crane for his comments and suggestions on this work. The authors are grateful to Charles Lee for his help in the Kummer function computing, Peter Wheelon for graphics work, and Roger Carlson for his technical editing of this article.

References

- [1] A. D. Wheelon, *Electromagnetic Scintillation II. Weak Scattering*, Cambridge, United Kingdom: Cambridge University Press, 2003.
- [2] V. I. Tatarskii, *The Effects of the Turbulent Atmosphere on Wave Propagation*, National Technical Information Office, U.S./ Department of Commerce, Springfield, Virginia, 1971.
- [3] J. Haddon and E. Vilar, "Scattering Induced Microwave Scintillations from Clear Air and Rain on Earth Space Paths and the Influence of Antenna Aperture," *IEEE Trans. Antennas Propagation*, vol. AP-34, no. 5, pp. 646–657, 1986.
- [4] C. Ho and A. Wheelon, "Amplitude Scintillation due to Atmospheric Turbulence for the Deep Space Network Ka-Band Downlink," *The Interplanetary Network Progress Report*, vol. 42-158, Jet Propulsion Laboratory, Pasadena, California, pp. 1–21, 2004. http://ipnpr/progress_report/42-158/158E.pdf

- [5] T. J. Mouldsley and E. Vilar, "Experimental and Theoretical Statistics of Microwave Amplitude Scintillations on Satellite Down-Link," *IEEE Trans. Antennas Propagation*, vol. AP-30, no. 6, pp. 1099–1106, 1982.
- [6] E. Vilar and J. Haddon, "Measurement and Modeling of Scintillation Intensity to Estimate Turbulence Parameters in an Earth-Space Path," *IEEE Trans. Antennas Propagation*, vol. AP-32, no. 4, pp. 340–346, 1984.
- [7] A. D. Wheelon, "Relation of Radio Measurements to the Spectrum of Tropospheric Dielectric Fluctuations," *J. Appl. Phys.*, vol. 28, no. 6, pp. 684–693, 1957.
- [8] R. Linfield, "The Effect of Aperture Averaging Upon Tropospheric Delay Fluctuations Seen With a DSN Antenna," *The Telecommunications and Data Acquisition Progress Report 42-124, October–December 1995*, Jet Propulsion Laboratory, Pasadena, California, pp. 1–7, February 15, 1996.
http://tmo.jpl.nasa.gov/tmo/progress_report/42-124/124A.pdf
- [9] R. K. Crane and D. V. Rogers, "Review of Propagation Results from the Advanced Communications Technology Satellite (ACTS) and Related Studies," *IEICE Trans. Commun.*, vol. E84B, no. 9, pp. 2357–2368, Japan, 2001.
- [10] C. E. Mayer, B. E. Jaegar, R. K. Crane, and X. Wang, "Ka-Band Scintillations: Measurements and Model Predictions," *Proc. IEEE*, vol. 85, no. 6, pp. 936–945, 1997.
- [11] D. C. Cox, H. W. Arnold, and H. H. Hoffman, "Observation of Cloud Produced Amplitude Scintillation on 19 and 28 GHz Earth-Space Paths," *Radio Sci.*, vol. 16, no. 5, pp. 885–907, 1981.

Appendix

Kummer Functions

The Kummer function, or confluent hypergeometric function, is generated when an integral has the following format:

$$\int_1^\infty e^{-zx} x^{b-a-1} (x-1)^{a-1} dx = e^{-z} \Gamma(a) U(a, b, z)$$

where the gamma function $\Gamma(a)$ is defined as

$$\Gamma(n) = \int_0^\infty x^{n-1} e^{-x} dx$$

and

$$\Gamma(n+1) = n\Gamma(n) = n!$$

The second type of Kummer function is denoted by $U(a, b, z)$ and is defined as

$$U(a, b, z) = \frac{\pi}{\sin(b\pi)} \left(\frac{M(a, b, z)}{\Gamma(1+a-b)\Gamma(b)} - z^{1-b} \frac{M(1+a-b, 2-b, z)}{\Gamma(a)\Gamma(2-b)} \right)$$

where $M(a, b, z)$ is the first function of the Kummer function and is defined as

$$M(a, b, z) = 1 + \frac{a}{b}z + \frac{a(a+1)}{b(b+1)} \frac{z^2}{2!} + \cdots + \frac{a_n}{b_n} \frac{z^n}{n!} + \cdots$$

Here

$$a_0 = 1$$

and

$$a_n = a(a+1)(a+2) \cdots (a+n-1)$$

with a similar expression for b_n .